AMERICAN METEOROLOGICAL SOCIETY
AMS Journals Online

AMS Home   Journals Home   Journal Archive   Subscribe   For Authors   Help   Advanced Search   [Search] Go

Full Text View

A Numerical Study of the Adjustment of a Narrow Stratified Current over a Sloping Bottom[*]

David C. Chapman

Woods Hole Oceanographic Institution, Woods Hole, Massachusetts

ABSTRACT

The adjustment of a narrow, stratified, cyclonic along-isobath current over a uniformly sloping bottom and the coupling between the current and the bottom boundary layer that develops beneath are investigated using a primitive-equation numerical model. The current generates a bottom Ekman layer immediately downstream of its origin, with downslope transport everywhere beneath the current, carrying lighter water under heavier water to produce a vertically well-mixed bottom boundary layer. At the top of the boundary layer, Ekman suction on the shallow side and pumping on the deep side lead to density advection in the vertical, tilted interior isopycnals, and thermal-wind shear of the interior along-isobath velocity. Flow above the bottom boundary layer is nearly perfectly geostrophic and along isopycnals. Buoyancy advection in the bottom boundary layer continues to cause growth of the boundary layer downstream, with subsequent reduction in bottom stress, until the flow reaches a steady downstream equilibrium beyond which only gradual changes occur as a result of viscosity and mixing.

The numerical results are compared with the idealized model of this adjustment process previously proposed by Chapman and Lentz. The same basic dynamics dominate, and some of the scales and parameter dependencies predicted by the idealized model apply to the numerical results. For example, the distance to the downstream equilibrium decreases with increasing buoyancy frequency and/or bottom slope, and the equilibrium structure is nearly independent of the bottom friction coefficient. The equilibrium bottom boundary layer thickness and the interior along-isobath velocity just above the boundary layer closely obey the idealized model scales; that is, the boundary layer thickness decreases with increasing buoyancy frequency and is independent of bottom slope, and the overlying current decreases while its width increases as either the buoyancy frequency or bottom slope decreases. However, the interior vertical shear in the numerical model tends to decouple the overlying current from the bottom boundary layer, so the structure of the bottom boundary layer in the downstream equilibrium is different from the idealized model, and neither the current width nor the surface currents are as sensitive to parameter variations as the idealized model suggests. Finally, the along-isobath current is not geostrophic near the bottom of the bottom boundary layer, as assumed in the idealized model, so the bottom boundary layer is not fully arrested, that is, bottom stress never quite vanishes downstream, suggesting that a completely frictionless downstream equilibrium is unlikely to be achieved.

Options:
- Create Reference
- Email this Article
- Add to MyArchive
- Search AMS Glossary

Search CrossRef for:
- Articles Citing This Article

Search Google Scholar for:
- David C. Chapman

1. Introduction

The importance of buoyancy advection in the bottom boundary layer and its influence on bottom stress have been the subject of numerous recent studies. The basic idea is as follows. An ocean current flowing over a frictional bottom generates a bottom boundary layer. If the ocean is stratified, horizontal velocities in the bottom boundary layer can transport buoyancy (i.e., heat and/or salt) laterally, thereby creating horizontal density gradients within the bottom boundary layer. On subinertial time scales, the horizontal density gradients lead to geostrophic vertical shear, which reduces the velocity near the bottom, thus altering the bottom stress and the development of the bottom boundary layer.

For the most part, this scenario has been investigated using one-dimensional models of bottom boundary layer behavior beneath a uniform and unbounded (in both horizontal and vertical directions) along-isobath flow in a uniformly stratified ocean [see the review by Garrett et al. (1993) and more recent papers by Ramsden (1995a,b) and Middleton and Ramsden (1996)]. These models nicely show how buoyancy advection in the bottom boundary layer reduces the bottom stress and the cross-isobath Ekman transport until the bottom appears frictionless to the overlying current. The boundary layer is then said to be "arrested."

One weakness of the one-dimensional models is the assumed lack of spatial variations in the along-isobath current that generates the bottom boundary layer. Vertical uniformity precludes the study of the adjustment of a vertically sheared current. Horizontal uniformity eliminates feedback between the boundary layer and the overlying current, and so precludes the study of a finite-width current in which both current and boundary layer are tightly coupled and adjust simultaneously. To address the latter limitation, Chapman and Lentz (1997, hereafter CL) developed an idealized three-dimensional steady model in which a finite-width cyclonic current (shallow water on the right looking downstream in the Northern Hemisphere) flows along a sloping bottom in a stratified, uniformly rotating fluid. As the flow moves downstream, bottom friction causes the current to spread laterally, but the spreading is limited by the developing bottom boundary layer, which reduces the bottom stress. Eventually the current reaches a downstream equilibrium in which bottom stress vanishes everywhere. The model provides a priori scales for the equilibrium structure, including current width, maximum boundary layer height, and velocities within the overlying current, all based on known parameters.

In some respects, the CL model represents a clear advance over the one-dimensional models, but it still requires numerous assumptions and approximations in its derivation, some of which are rather severe. Most notably, (i) the along-isobath current is assumed to be in geostrophic balance everywhere, even throughout the bottom boundary layer; (ii) the current above the bottom boundary layer is assumed to remain vertically uniform (i.e., without vertical shear); (iii) density within the bottom boundary layer is assumed to be completely vertically mixed; and (iv) nonlinear momentum advection is ignored. The appropriateness of these assumptions in more realistic settings is unclear. Therefore, to relax some of these assumptions, a primitive-equation numerical model is used to study the adjustment of a vertically uniform, narrow current as it encounters a sloping bottom, much like that of the CL model. Some aspects of the model remain highly idealized (e.g., vertically uniform inflow). Nevertheless, the calculations serve both to examine the adjustment dynamics in the framework of more complete physics, and to test the applicability of the idealized CL model in more realistic situations.

It is important to bear in mind that the adjustment process in the numerical calculations is intrinsically more complicated than in either the one-dimensional models or the CL model. The one-dimensional models ignore lateral spatial variations and consider only temporal adjustment, while the steady CL model considers only spatial adjustment of an upstream source. On the other hand, both spatial and temporal adjustments occur simultaneously in the numerical calculations, making it difficult to separate the two in a simple way. Initially there are elements of the classic time-dependent, frictional, spinup process and bottom boundary layer development, but these aspects are lost as the flow approaches a steady state. Furthermore, spatial and temporal changes can combine to produce new features not found in either the one-dimensional models or the CL model.

In section 2, the numerical model and the calculations are described. The dynamics of the adjustment process are examined in section 3. Following CL, only cyclonic currents are considered, this being the natural direction for large-scale flows that are not wind-driven. The results are compared with the idealized CL model in section 4. Some discussion and a summary follow in sections 5 and 6, respectively.

2. Numerical model

The *s*-coordinate primitive-equation model (SPEM5.1), developed by D. Haidvogel's group at Rutgers University, is used to solve the following hydrostatic and Boussinesq momentum, density and continuity equations:

$$\rho_t + \mathbf{u} \cdot \nabla\rho = (K_V \rho_z)_z + F_\rho \qquad (4)$$

$$\nabla \cdot \mathbf{u} = 0. \qquad (5)$$

In this system (u, υ, w) represent the (x, y, z) components of the velocity $\mathbf{u}$ with z directed vertically upward from the ocean surface, ρ is the difference between the total density and a constant reference density ρ_0, p is pressure, f is the Coriolis parameter, g is gravitational acceleration, A_V is the vertical eddy viscosity, K_V is the vertical eddy diffusivity, and t is time. Variables $F_{u,\upsilon,\rho}$ represent dissipative functions that are required for numerical stability. Subscripts x, y, z, and t denote partial differentiation.

In many respects, SPEM5.1 is nearly the same as earlier versions of SPEM (e.g., Haidvogel et al. 1991). Important differences are that SPEM5.1 approximates the system (1)–(5) with finite differences in both horizontal and vertical directions, and a generalized stretched vertical coordinate [the s coordinate described by Song and Haidvogel (1994)] allows greater flexibility in specifying the locations of vertical grid points. For the present calculations, the grid points are concentrated near the bottom, in order to resolve the bottom boundary layer, by using the following s-coordinate mapping:

$$z(s) = h_c s + (h - h_c)\{\sinh[\theta(s + 1)]/\sinh\theta - 1\}, -1 \leqslant s \leqslant 0,(6)$$

where $h(x, y)$ is the bottom depth, h_c is the shallowest depth, and θ is a prescribed constant.

The model domain is a uniformly rotating ($f = 10^{-4}$ s^{-1}) straight channel with solid walls at $y = 0$ and $y = 400$ km and open boundaries at $x = 0$ and $x = 600$ km (Fig. 1 ⊙). The horizontal grid typically has 128 points in each direction, distributed uniformly over the region $0 \leqslant x \leqslant 300$ km and $0 \leqslant y \leqslant 270$ km, within which $\Delta x = 3.82$ km and $\Delta y = 2.72$ km. Outside this region, the grid spacing increases smoothly toward the boundaries with maximum spacings of $\Delta x = 10.3$ km and $\Delta y = 8.03$ km. The bottom is uniformly sloping from a minimum depth of $h_c = 50$ m along $y = 0$ to a maximum depth of 400 m, beyond which the bottom is flat. Vertical resolution varies with depth according to (6) with 30 grid points. At the shallowest depth ($h = h_c$ at $y = 0$) the grid spacing is uniform with $\Delta z = 1.72$ m. The choice of $\theta = 2.5$ in (6) yields smaller grid spacing near the bottom at all depths such that, where $h = 400$ m, $\Delta z = 6.5$ m at the bottom and $\Delta z = 30$ m at the surface. The flows considered here do not reach depths below about 300 m, so they are reasonably well resolved throughout. Doubling the resolution at the bottom ($\theta = 5$) produces no noticable changes in the results.

Each calculation begins with a stably stratified, quiescent ocean characterized by a constant buoyancy frequency $N = (-g\rho_z/\rho_0)^{1/2}$. A narrow, vertically uniform inflow is prescribed at the upstream boundary ($x = 0$), centered over the 200-m isobath with constant velocity u_0 and width $2W_0$. As mentioned above, this choice is not particularly realistic, but it allows both the study of finite-width effects and comparison with the CL model. Other features, such as vertical shear in the prescribed inflow, must await future studies. All variables on this open boundary remain fixed at their intial values throughout the calculation. A radiation condition similar to that described by Chapman and Haidvogel (1992) is applied at the downstream boundary ($x = 600$ km). First, the interior barotropic vorticity is advected to the boundary (zero-gradient condition) and used to compute the barotropic stream function there (after assuming that the curvature of the stream function in x vanishes). Then a zero-gradient condition is applied to the interior density and depth-varying velocities. This condition produces better results than a purely wave-like radiation condition and/or a sponge, presumably because of the advective nature of the interior flows. The most significant effect of this imperfect open boundary condition is the generation of baroclinic Kelvin waves (primarily first mode) that move along the deep boundary in the $-x$ direction toward the inflow boundary where they continue around the corner and affect the adjustment of the inflow. These Kelvin waves are effectively eliminated by applying a Rayleigh-damping sponge along the entire deep boundary, 320 km $\geq y \geq 400$ km (shaded region in Fig. 1 ⊙).

There are no fluxes of density or momentum at the surface or the solid sidewalls. At the bottom, the density flux is zero, while the shear stress is specified using a linear bottom friction parameterization,

$$A_V u_z = ru; \qquad A_V \upsilon_z = r\upsilon \quad \text{at } z = -h,(7)$$

where r is a bottom friction coefficient.

The vertical mixing coefficients are approximated using a Richardson-number dependent scheme:

$$A_V = 0.00001 + \frac{0.00099}{(1.0 + 0.3\text{Ri})^{1/2}} \qquad (8)$$

$$K_V = 0.00001 + \frac{0.00099}{(1.0 + 0.3\text{Ri})^{3/2}}, \qquad (9)$$

where the units are m^2 s^{-1} and the Richardson number is defined by Ri $= N^2/[(u_z)^2 + (\upsilon_z)^2]$. Thus, the mixing

coefficients are in the range 10^{-5} to 10^{-3} m^2 s^{-1}. Tests using other schemes for estimating A_V and K_V (e.g., standard Pacanowski–Philander or Mellor–Yamada Level 2) produce nearly identical results provided that A_V and K_V remain within the same range. Otherwise, locally enormous values can generate high spatial variability and/or numerical inaccuracies in the finite-difference approximations. Additional vertical mixing of density is applied in the form of instantaneous convective adjustment whenever the water column becomes statically unstable (i.e., when lighter water appears under heavier water). In the present calculations, this occurs only within the bottom boundary layer.

For numerical stability, Laplacian subgridscale mixing with constant mixing coefficients is applied along horizontal surfaces (i.e., $F_{u,\upsilon,\rho} = v_{u,\upsilon,\rho} \nabla^2 u, \upsilon, \rho$), using the smallest mixing coefficients that produce stable calculations; $v_{u,\upsilon} = 50$ m^2 s^{-1} and $v_\rho = 10$ m^2 s^{-1}.

Each calculation continues until the flow appears to have reached a steady state everywhere in the region of uniform grid spacing ($0 \leqslant x \leqslant 300$ km, $0 \leqslant y \leqslant 270$ km). This typically requires between 150 and 200 days of simulation time, varying somewhat with model parameters. The time step is 432 seconds.

3. Adjustment

The adjustment of the imposed inflow depends primarily on the buoyancy frequency N, bottom slope α, bottom friction coefficient r, inflow velocity u_0, and width W_0. The range of choices for each variable is restricted by both limited domain size and computational cost. That is, the flow must adjust within about 300–400 km downstream without reaching the sidewalls. Further, the inflow should be swift enough for the adjustment to occur within a reasonable simulation time, but not so swift as to be highly nonlinear and/or unstable. The inflow should also be narrow enough for the adjustment to substantially widen the flow in order to test the scales of the CL model. After numerous trials, the most appropriate compromise seemed to be to fix the inflow at $u_0 = 0.1$ m s^{-1} with a width of $2W_0 = 32.6$ km, and to vary the other parameters. One weakness of this choice is that the adjusted downstream flows are rather slow owing to the lateral spreading of the inflow. Nevertheless, this choice allows the adjustment process to be examined and compared with CL without introducing strong nonlinearities. The buoyancy frequency ranges from $N = 0$ to 18×10^{-3} s^{-1}, while the bottom slope varies from $\alpha = 0.001$ to 0.002. The maximum Burger number considered is $N\alpha/f = 0.18$, which represents relatively weak stratification. This implies that the vertical scale of the flow should be greater than the total water depth and that the dynamics should be linear, as argued by CL. The bottom friction coefficient varies from $r = 0.0005$ to 0.002 m s^{-1}. Other parameters were varied for a few calculations which are mentioned below.

Within the ranges of parameters considered, the qualitative results are remarkably robust. That is, the adjustment process is nearly identical for all cases, with only the quantitative details differing substantially. Therefore, the adjustment process for a typical calculation is described next; first the fully adjusted, nearly steady flow, and then the temporal development that leads to the steady flow. This is followed by a few examples of the changes introduced by other parameter choices.

a. Steady flow

For the standard calculation, $N = 9 \times 10^{-3}$ s^{-1}, $\alpha = 0.001$ (giving $N\alpha/f = 0.09$), and $r = 0.002$ m s^{-1}. The numerical model is run for 200 days. Figure 2 ⊙ shows plan views of the horizontal velocities at the surface and the along-isobath velocity at the bottom after 200 days. (Note that only a portion of the model domain is shown in this and subsequent plots.) The along-isobath surface velocity u^s decreases downstream as the current widens and the core moves into deeper water. The along-isobath bottom velocity u^b decreases more rapidly, falling below 0.01 m s^{-1} after only 50 km, indicating a marked reduction in bottom stress. The cross-isobath surface velocity υ^s is convergent toward the inflow within about 30–50 km downstream, beyond which the sign changes to a widening or spreading flow that slows downstream. The pattern is asymmetric with larger positive velocities, consistent with the overall shifting of the current to deeper water.

Figure 3 ⊙ shows vertical sections of the three velocity components and the density field at $x = 300$ km where the current has evolved to a structure that changes only slightly farther downstream. Qualitatively, this flow resembles the CL model and may be considered a "downstream equilibrium" structure. The along-isobath velocity is concentrated roughly between $y = 110$ to 230 km, with a maximum at about $y = 180$ km and a well-developed bottom boundary layer as thick as 50 m beneath, much greater than the Ekman layer thickness of about 10 m. The cross-isobath velocity is small and directed toward deeper water over most of the water column, consistent with Fig. 2 ⊙, while the vertical velocity is small nearly everywhere. However, there are several important additional features to note. First, the isopycnals above the bottom boundary layer are not quite horizontal. Although difficult to see in Fig. 3 ⊙, the isopycnals beneath the core of the along-isobath current ($y \approx 190$ km, -180 m $< z < -100$ m) are raised several meters, coincident with the vertical shear in u. Second, the bottom boundary layer is not completely vertically mixed on the deep side of the current. Third, both υ and w indicate a downslope flow close to the bottom within the bottom boundary layer, suggesting that the boundary layer is not fully arrested.

The circulation within this steady flow is, for the most part, fairly simple and could be anticipated from the classic spinup of a stratified fluid (e.g., Pedlosky 1987). Immediately downstream of the inflow, an Ekman layer is established. Stratification effects are minimal here, so the numerical horizontal velocities are close to the theoretical Ekman solution for

an unstratified flow, found using the bottom boundary condition (7) as applied by SPEM5.1 (Fig. 4 ⊙; see the appendix for details). The downslope Ekman transport ($v > 0$ in Fig. 4 ⊙) pushes lighter water under heavier water and generates a well-mixed bottom boundary layer. The downslope transport is supplied by Ekman suction into the boundary layer on the shallow side, and it produces Ekman pumping out of the boundary layer on the deep side. The resulting large vertical velocities near the inflow (Fig. 5 ⊙) raise (lower) the isopycnals over the deep (shallow) side of the boundary layer. Tilted interior isopycnals lead to thermal-wind shear in the along-isobath velocity such that u decreases toward the bottom. This, in turn, tends to reduce the bottom stress and, thus, the Ekman transport, suction, and pumping. Interior vertical velocities, therefore, decrease rapidly downstream (Fig. 5 ⊙), leaving the downstream equilibrium shown in Fig. 3 ⊙.

Bottom boundary layer growth and subsequent reduction in downslope transport are evident in an along-isobath section of density and cross-isobath velocity through the center of the current (Fig. 6 ⊙). The uplifting of isopycnals caused by strong vertical velocites near the inflow ($x < 50$ km) is clearly evident. Downstream of this adjustment region, the isopycnals are basically horizontal in the along-isobath direction. The well-mixed bottom boundary layer grows downstream, while the cross-isobath velocity in the boundary layer decreases, approaching zero as the boundary layer reaches its full height (at about $x = 250$ km).

b. Temporal development

The temporal development of the fully adjusted steady flow is not as straightforward as the steady flow itself. There are two phases for the adjustment at any fixed downstream location. The first phase begins immediately after the calculation starts, as information of the imposed inflow propagates rapidly downstream in the form of topographic Rossby waves. (The barotropic wave arrives instantly owing to the rigid lid.) During this phase, the bottom Ekman layer and associated well-mixed boundary layer form locally much like the one-dimensional models mentioned in the introduction. The second phase begins when information of the vertical shear associated with the tilted interior isopycnals arrives. This information is advected downstream at roughly the speed of the interior velocity; that is, density advection along isobaths plays a leading dynamical role. The onset of the second phase leads fairly quickly to the steady-state flow described above. The time to reach steady state varies spatially, depending on the duration of the first phase, so comparisons with previous adjustment timescale estimates based on, for example, one-dimensional models are of questionable value.

Time histories of surface velocity u^s and bottom stress ru^b at three points along the center of the current illustrate the two adjustment phases (Fig. 7 ⊙). Initially, bottom stress decreases steadily in response to the growing bottom boundary layer which slows the downslope Ekman transport as in the one-dimensional models (see below). However, before shutdown is complete, the altered interior flow (i.e., uplifted isopycnals) arrives and essentially halts the further evolution of the boundary layer. This transition from phase one to phase two is marked by a distinct change in u_s at each location; after about 30 days at $x = 100$ km, then after about 60 days at $x = 200$ km, and finally after about 90 days at $x = 300$ km. Both surface velocity and bottom stress then tend toward constants in time, indicating that the steady state is being approached. The times of the transition at these locations indicate an advection speed of about 0.038 m s^{-1}, well within the range of interior velocities in Fig. 7a ⊙.

The transition is also marked by a change from ageostrophic to nearly geostrophic flow along isopycnals (except in the bottom boundary layer). This may be illustrated by considering the equations of motion for steady flow that is everywhere in thermal-wind balance and nondiffusive. In this case, (1)–(5) reduce to

$$v_z = -g\rho_x/\rho_0 f; \qquad u_z = g\rho_y/\rho_0 f \qquad (10)$$
$$u\rho_x + v\rho_y + w\rho_z = 0. \qquad (11)$$

These balances can be combined, as done by Schott and Stommel (1978), to obtain

$$uv_z - vu_z = wg\rho_z/\rho_0 f. \quad (12)$$

If the flow is both geostrophic and along isopycnals, then (12) should be satisfied. Figure 8 ⊙ shows vertical sections of $|\tanh(\xi - 1)|$ where $\xi = (wg\rho_z/\rho_0 f)/(uv_z - vu_z)$ at $x = 100$ km for several times during the standard calculation. Values of zero (black) indicate that $\xi = 1$, so (12) is satisfied. The $u = 0.01$ m s^{-1} contour encompasses the bulk of the along-isobath current showing that the current width is established early in the calculation. The bottom boundary layer appears as a region of uniform gray at the bottom of the current where (12) is not satisfied because vertical diffusion of momentum is important. These sections are at the same along-isobath location as the dash–dot curves in Fig. 7 ⊙. After 30 days, the flow is in the transition, and (12) is not generally satisfied within the current. By day 60, the second phase of adjustment is underway and some of the interior current satisfies (12). By day 150, nearly all of the flow above the bottom boundary layer satisfies (12), and the flow is nearly steady. The adjustment is similar at other downstream locations. In the steady state, nonlinear advection of momentum is important only in a small region near the inflow and within 10–20 km of the edges of the current.

During the first phase, the bottom boundary layer develops beneath the inflow essentially like the one-dimensional models. Downslope Ekman transport carries lighter water under heavier water, which then mixes vertically by convective adjustment

to create a thick boundary layer that extends well above the Ekman layer. An example is shown in Fig. 9 ⚪, at $x = 300$ km and $y = 180$ km, corresponding to the thickest part of the boundary layer shown in Fig. 3 ⚪ and to the solid curves in Fig. 7 ⚪. As the boundary layer grows, a region of fairly constant shear in u develops that is in thermal-wind balance with the horizontal density gradients within the boundary layer (from $z = -220$ m to the top of the boundary layer). The height of the constant shear layer increases as the boundary layer grows, but it never extends to the bottom through the Ekman layer. The downslope velocities (and transport) decrease in conjunction with the shear layer growth. This behavior continues for about 100 days until the tilted interior isopycnals arrive (transition to phase two). Boundary layer growth then slows as the interior current shear increases, and the steady state is approached.

The behavior at the deep side of the current is somewhat different, as shown in Fig. 10 ⚪ at $x = 300$ km and $y = 210$ km. Initially, the bottom boundary layer develops as described above; an Ekman layer forms which transports light water downslope, creating a thickening boundary layer. The situation then becomes more complex. The decrease of the overlying interior along-isobath flow toward the deep side of the current creates a local convergence in Ekman transport within the bottom boundary layer. The resulting accumulation of buoyancy causes rapid growth of the boundary layer, which quickly reduces the bottom velocity (and, therefore, bottom stress) to zero. However, instead of remaining in the arrested state, the boundary layer grows slightly beyond the thickness for shut-down, and basically "overshoots" to produce a reversal in u at the bottom with *upslope* Ekman transport ($\mathcal{U} < 0$). Heavier water is now pushed under lighter water, stabilizing the water column and creating a weakly stratified bottom boundary layer. Thus, the bottom boundary layer beneath the deep side of the current in Fig. 3 ⚪ remains incompletely mixed, and both u and $\mathcal{U}$ reverse near the bottom there.

c. Parameter variations

The adjustment just described is qualitatively identical for all combinations of parameters considered, although the details may vary. For example, Fig. 11 ⚪ shows the along-isobath bottom stress ru^b beneath the core of the current at steady state for several combinations of parameters. The thick solid curve is the standard calculation described above. As expected, based on CL, increased stratification and/or steeper bottom slope lead to more rapid downstream adjustment because of increased buoyancy advection in the bottom boundary layer. Changes in r have little effect on the downstream reduction in bottom stress. Basically, reduced r produces larger bottom velocities u^b in the Ekman layer near the inflow such that the bottom stress ru^b remains nearly unchanged. Note that the bottom stress approaches a small value but never vanishes; there is always an increased shear near the bottom associated with the Ekman layer (see Fig. 9 ⚪).

The temporal development of bottom stress at a fixed point clearly shows the effects of buoyancy advection in the bottom boundary layer (Fig. 12 ⚪). With no stratification, the bottom stress at $x = 300$ km and $y = 180$ km increases over the first 30 days and becomes a constant thereafter. The lack of stratification precludes shut-down of the bottom boundary layer. With weak stratification, bottom stress first increases and then gradually decreases with time, indicating a slight tendency for shutting down. Stronger stratification produces a substantially more rapid decrease in bottom stress to a much smaller value, that is, close to being arrested.

A few calculations were made with different inflow configurations, always keeping the flow narrow and slow enough that the current would widen downstream and remain stable. Again, the behavior is qualitatively the same. The primary effect of changing the inflow velocity u_0 is to change the vertical displacement of isopycnals just downstream of the inflow. For example, an inflow of half the width and twice the velocity of the standard case ($2W_0 = 16.3$ km, $u_0 = 0.2$ m s^{-1}) produces about twice the downslope Ekman transport in the bottom boundary layer, which causes about twice the Ekman suction and pumping, and about twice the vertical displacement of isopycnals in the interior. As a result, vertical shear above the bottom boundary layer is increased, and the thermal-wind shear in the boundary layer is not such a distinctive feature in the downstream equilibrium (Fig. 13 ⚪). Nevertheless, the height and width of the boundary layer in the downstream equilibrium are nearly unchanged.

4. Comparisons with CL

The results of the previous section show both similarities and differences between the numerical calculations and the idealized CL model. For example, the adjustment process in the numerical model, especially the first phase, is quite similar to that assumed by CL. As the bottom boundary layer grows beneath the widening overlying current, buoyancy advection in the bottom boundary layer alters the adjustment of the current, and both boundary layer and interior flows adjust to a downstream equilibrium flow that persists with little further change in structure. However, contrary to the CL model, the interior flow in the numerical calculations becomes vertically sheared (phase two), with corresponding displacement of isopycnals, leading to weaker coupling of the interior and boundary layer flows. Furthermore, bottom stress in the numerical calculations does not vanish downstream (Fig. 11 ⚪), so the bottom boundary layer is not truly arrested. In addition, the overshooting of the bottom boundary layer on the deep side of the current dramatically alters the cross-isobath flow there, so the boundary layer remains stratified as described above.

A quantitative comparison of the scales and parameter dependencies of the CL model with those of the numerical model is not entirely straightforward. For example, it is unclear how to define the bottom boundary layer in the numerical model. One definition might be the height above the bottom to which density is completely mixed. However, this definition ignores the clear influence of the bottom boundary layer on the deep side of the current (Figs. 3 ⚪ and 10 ⚪) where some stratification remains all the way to the bottom. On the other hand, the height to which this influence is important is difficult to quantify. As an alternative, the bottom boundary layer thickness in the numerical results δ_n is defined here as the vertical

displacement of isopycnals from their initial state that produces the density at the bottom ρ^b in the downstream equilibrium:

$$\delta_n = h - g\rho^b/\rho_0 N^2. \quad (13)$$

This definition is equivalent to that of CL where the boundary layer is vertically well mixed, but it may underestimate the vertical extent of the boundary layer influence in regions of incomplete vertical mixing. Similarly, the interior vertical shear in the numerical model makes it unclear which velocity should be compared with the overlying current of CL, so both the surface velocity and the velocity just above the bottom boundary layer (on an s-coordinate surface) are compared with that of the CL model.

Figure 14 compares the downstream equilibrium structure from the standard numerical calculation (Fig. 3) with the equivalent CL model. The bottom boundary layer in the numerical solution has a minimum thickness of about 8 m away from the overlying current, caused by both the bending of isopycnals near the bottom to satisfy the requirement of no density flux through the bottom and the resulting downslope current near the bottom (cf. Fig. 3). Otherwise, the width and maximum thickness of the boundary layer are comparable to the CL model, although the shape is different. The velocity structures are remarkably similar in width and magnitude. The smooth edges in the numerical results are caused by viscosity and mixing. The full density field comparison clearly shows the uplifted interior isopycnals of the numerical results and the lack of complete vertical mixing on the deep side of the boundary layer.

To compare the parameter dependencies from the CL model with the numerical results, the boundary layer height, maximum along-isobath velocity and current width (from plots like Fig. 14) are estimated for various combinations of parameters. In each case, the quantities are estimated at the downstream location where bottom stress reaches its minimum (e.g., Fig. 11), beyond which changes in current structure are slight. The current width is defined as half the distance between the y locations on each side of the current where the interior velocity reaches 10% of the maximum. The CL scales for boundary layer thickness, along-isobath velocity and current width are, respectively,

$$\delta \sim \left(\frac{f}{N}\right)\left(\frac{2u_0 W_0}{f}\right)^{1/2}, \qquad u^i \sim N\alpha\left(\frac{2u_0 W_0}{f}\right)^{1/2},$$

$$W \sim \left(\frac{f}{N\alpha}\right)\left(\frac{2u_0 W_0}{f}\right)^{1/2}. \qquad (14)$$

Figure 15 shows a comparison of these CL scales with the numerical results for eight calculations listed in Table 1. (Note that runs 4 and 7 have identical W_n and δ_n, so it appears that only seven points are plotted in the top and bottom panels.) The solid line in each panel is the least squares fit that passes through the origin (i.e., each scale should vanish simultaneously). The magnitudes are unimportant here because (14) only provides the parameter dependencies, so the extent to which the points fall on the lines is an indication of their agreement with (14). The boundary layer thickness agrees quite well with (14); δ_n is inversely related to the buoyancy frequency and independent of bottom slope. The along-isobath current just above the boundary layer closely follows (14), increasing with an increase in either buoyancy frequency or bottom slope. However, the surface velocity does not follow (14), indicating the decoupling of the interior flow from the boundary layer associated with the interior vertical shear. As a result, the current width is not nearly as sensitive to changes in stratification and bottom slope as the CL model suggests.

5. Discussion

The idealized CL model was an attempt to understand the dynamical feedback in three dimensions between a narrow stratified flow over a sloping bottom and the bottom boundary layer that grows beneath it. Numerous assumptions placed strong constraints on the properties of the flow, but allowed solutions to be easily obtained and provided scales relating the flow structure to the prescribed model parameters. The numerical calculations presented here show that the CL model captures the essence of the feedback dynamics, but also that several of the CL simplifications are overly restrictive and lead to substantial changes in the current structure.

One important difference between the CL model and the numerical results concerns vertical shear of the interior flow. The CL model assumes no interior vertical shear (i.e., horizontal isopycnals), so interior fluid moves like Taylor columns riding on top of the bottom boundary layer. However, in the numerical model, Ekman suction and pumping at the top of the bottom boundary layer just downstream from the inflow displaces the interior isopycnals (Figs. 5 and 6). The vertical shear associated with the tilted isopycnals then continues downstream with the current, so the interior flow is not restricted to move as columns and is less tightly coupled to the bottom boundary layer. In other words, the boundary layer responds to the along-isobath current just above it essentially as predicted by the CL model, but the surface velocity is different because of the interior vertical shear and does not follow the CL predictions so closely (Fig. 15). As a result, the downstream equilibrium is altered and the current width is not as sensitive to changes in the model parameters as expected from the CL model. The importance of interior vertical shear underscores the need for additional modeling studies in order to apply these ideas to ocean currents, such as deep western boundary currents or poleward undercurrents, in which vertical shear plays a dominant dynamical role.

Another important assumption made for the CL model is that the along-isobath flow is geostrophic everywhere. This is a

good approximation for the numerical results except in the bottom Ekman layer where the cross-isobath bottom stress is important. To test the importance of this bottom stress term, the standard numerical calculation was repeated with $A_V \partial \upsilon / \partial z$ = 0 at $z = -h$ instead of the second part of (7). The primary effect is that bottom velocities near the inflow (especially υ^b) are much larger than they were with the bottom stress term included (Fig. 16 ⊙⮞). This produces substantially stronger Ekman suction and pumping, greater displacement of interior isopycnals and stronger interior vertical shear. The flow forms a downstream equilibrium within 150 km with a stronger surface flow. The flow is still similar to the CL model, but the interior vertical shear is even more important. Thus, the neglect of cross-isobath bottom stress is not a particularly good assumption.

Despite the rapid downstream decrease in bottom stress, the bottom boundary layer is never fully arrested in any of the numerical calculations. Instead, a nearly perfect Ekman momentum balance, with a small amount of cross-isobath transport, always remains near the bottom. The reason for this is not clear, but it is consistent with some one-dimensional calculations of Middleton and Ramsden (1996; e.g., their Fig. 2). Several calculations were made with other schemes for estimating vertical mixing coefficients, such as Pacanowski–Philander and Mellor–Yamada Level 2, but bottom stress never vanished. This suggests that there may always be some circulation within the bottom boundary layer and that the overlying current will experience some frictional decay, albeit slight. Furthermore, the overshooting of the bottom boundary layer response on the deep side of the current produces some upslope Ekman transport and a slightly stratified boundary layer. It is interesting to note that Pickart (2000) finds vertical density stratification within the bottom boundary layer beneath the shelfbreak jet in the Middle Atlantic Bight, similar to that on the deep side of the current in the present calculations.

An interesting feature of some of the calculations that was not mentioned above (and will not be investigated thoroughly here) is the occasional appearance of short-scale, wavelike patterns in the bottom boundary layer on the deep side of the current. These features tend to occur at the leading edge of the advective signal that initiates the transition from phase one to phase two of the adjustment process (see section 3b). To determine whether they might be numerical instabilities occurring where bottom stress is small, the standard calculation was repeated with increased resolution. An example with twice the resolution of the standard case (Fig. 17 ⊙⮞) shows that the features are not only present but better resolved, indicating that they are probably not numerical artifacts. The wave-like features have horizontal scales of about 10–20 km, and vertical scales of about 50 m with strong vertical and horizontal velocities. They appear similar in structure to the two-dimensional symmetric instabilities analyzed by Allen and Newberger (1998), but the horizontal scales here are considerably larger. They could perhaps be three-dimensional versions of Allen and Newberger's instabilities, but this remains to be investigated. In any case, they do not seem to alter the steady-state downstream equilibrium. For example, the waves in Fig. 17 ⊙⮞ move beyond $x = 300$ km by day 200. Their role in the adjustment process remains a mystery.

6. Summary

A primitive-equation numerical model has been used to investigate the adjustment of a narrow, stratified, along-isobath current over a sloping bottom and the coupling between the overlying current and the bottom boundary layer that develops beneath. The current generates a bottom Ekman layer immediately downstream of its origin, with downslope transport everywhere beneath the current, carrying lighter water under heavier water to produce a vertically well-mixed bottom boundary layer. At the top of the boundary layer, Ekman suction on the shallow side and pumping on the deep side lead to density advection in the vertical, tilted interior isopycnals, and thermal-wind shear of the interior along-isobath velocity. Flow above the bottom boundary layer is nearly perfectly geostrophic and along isopycnals. Buoyancy advection in the bottom boundary layer continues to cause growth of the boundary layer downstream, with subsequent reduction in bottom stress, until the flow reaches a steady downstream equilibrium beyond which only gradual changes occur as a result of viscosity and mixing.

The numerical results are qualitatively similar to the idealized model of Chapman and Lentz (1997). The same basic dynamics dominate, and some of the scales and parameter dependencies predicted by the CL model apply to the numerical results. For example, the distance to the downstream equilibrium decreases with increasing buoyancy frequency and/or bottom slope, and the equilibrium structure is nearly independent of the bottom friction coefficient. The equilibrium bottom boundary layer thickness and the interior along-isobath velocity just above the bottom boundary layer closely obey the CL scales; that is, the boundary layer thickness decreases with increasing buoyancy frequency and is independent of bottom slope, and the overlying current decreases while its width increases as either the buoyancy frequency or bottom slope decreases. Also, nonlinear momentum advection is dynamically unimportant except within a short distance downstream from the inflow.

However, there are some important differences between the numerical results and the CL model. First, the interior vertical shear in the numerical model, to some extent, decouples the overlying current from the bottom boundary layer, so the structure of the downstream equilibrium is altered. In particular, the structure of the bottom boundary layer is different, and neither the current width nor the surface currents are as sensitive to parameter variations as the CL model suggests. Second, the along-isobath current is not geostrophic through the entire bottom boundary layer, as assumed in the CL model. There is always an additional shear stress contribution near the bottom that prevents the bottom boundary layer from being fully arrested, that is, bottom stress never quite vanishes downstream. Finally, the bottom boundary layer remains slightly stratified on the deep side of the current, owing to a local reversal in the Ekman transport.

The CL model captures the essence of the feedback between the bottom boundary layer and the overlying current, but some restrictive assumptions make the coupling overly tight. Therefore, the CL model may be useful for providing insight and estimates of some current properties, but the details of the flow are more complicated and require some relaxation of the assumptions in CL. The numerical results provide a more dynamically consistent view of the adjustment process.

REFERENCES

Allen, J. S., and P. A. Newberger, 1998: On symmetric instabilities in oceanic bottom boundary layers. *J. Phys. Oceanogr.,* **28,** 1131–1151. Find this article online

Chapman, D. C., and D. B. Haidvogel, 1992: Formation of Taylor caps over a tall isolated seamount in a stratified ocean. *Geophys. Astrophys. Fluid Dyn.,* **64,** 31–65.

— , and S. J. Lentz, 1997: Adjustment of stratified flow over a sloping bottom. *J. Phys. Oceanogr.,* **27,** 340–356. Find this article online

Garrett, C., P. MacCready, and P. Rhines, 1993: Boundary mixing and arrested Ekman layers: Rotating stratified flow near a sloping boundary. *Annu. Rev. Fluid Mech.,* **25,** 291–323.

Haidvogel, D., J. Wilkin, and R. Young, 1991: A semi-spectral primitive equation ocean circulation model using vertical sigma and orthogonal curvilinear horizontal coordinates. *J. Comput. Phys.,* **94,** 151–185.

Middleton, J. F., and D. Ramsden, 1996: The evolution of the bottom boundary layer on the sloping continental shelf: A numerical study. *J. Geophys. Res.,* **101,** 18 061–18 077.

Pedlosky, J., 1987: *Geophysical Fluids Dynamics.* 2d ed. Springer-Verlag, 710 pp.

Pickart, R. S., 2000: Bottom boundary layer structure and detachment in the shelfbreak jet of the Middle Atlantic Bight. *J. Phys. Oceanogr.,* **30,** 2668–2686. Find this article online

Ramsden, D., 1995a: Response of an oceanic bottom boundary layer on a slope to interior flow. Part I. Time-independent interior flow. *J. Phys. Oceanogr.,* **25,** 1672–1687. Find this article online

— , 1995b: Response of an oceanic bottom boundary layer on a slope to interior flow. Part II. Time-dependent interior flow. *J. Phys. Oceanogr.,* **25,** 1688–1695. Find this article online

Schott, F., and H. Stommel, 1978: Beta spirals and absolute velocities in different oceans. *Deep-Sea Res.,* **25,** 961–1010.

Song, Y., and D. Haidvogel, 1994: A semi-implicit ocean circulation model using a generalized topography-following coordinate system. *J. Comput. Phys.,* **115,** 228–244.

APPENDIX

7. Bottom Ekman Layer in SPEM5.1

The stress boundary condition (7) is not actually applied at $z = -h$ in SPEM5.1 because the horizontal velocities are defined on a vertically staggered grid such that they are unknown at $z = -h$. Instead, the velocities on the right-hand sides in (7) are evaluated at $z = -h + \Delta z_0$, where Δz_0 is half the distance from the bottom to the first w grid point above the bottom.

In the present calculations, this distance is small, but it still affects the structure of the bottom boundary layer. To demonstrate, the standard unstratified Ekman layer over a flat bottom (e.g., Pedlosky 1987, p. 185) can be solved, using (7) with the right-hand sides evaluated at $z = -h + \Delta z_0$, to obtain

$$u = U\left\{1 - e^{-(z+h)/\delta_E}\left[A_1 \cos\left(\frac{z+h}{\delta_E}\right) - A_2 \sin\left(\frac{z+h}{\delta_E}\right)\right]\right\}$$

(A1)

$$v = Ue^{-(z+h)/\delta_E}\left[A_1 \sin\left(\frac{z+h}{\delta_E}\right) + A_2 \cos\left(\frac{z+h}{\delta_E}\right)\right], \quad \text{(A2)}$$

where U is the overlying current, and $\delta_E = (2A_V/f)^{1/2}$ is the Ekman layer scale. The constants A_1, A_2 are

$$A_1 = \frac{\beta + e^{-\Delta z_0/\delta_E}\cos(\Delta z_0/\delta_E)}{[\beta + e^{-\Delta z_0/\delta_E}\cos(\Delta z_0/\delta_E)]^2 + [\beta - e^{-\Delta z_0/\delta_E}\sin(\Delta z_0/\delta_E)]^2} \tag{A3}$$

$$A_2 = \frac{\beta - e^{-\Delta z_0/\delta_E}\sin(\Delta z_0/\delta_E)}{[\beta + e^{-\Delta z_0/\delta_E}\cos(\Delta z_0/\delta_E)]^2 + [\beta - e^{-\Delta z_0/\delta_E}\sin(\Delta z_0/\delta_E)]^2}, \tag{A4}$$

where $\beta = (fA_V/2r^2)^{1/2}$. The standard Ekman solution, with (7) applied at the bottom, is recovered by setting $\Delta z_0 = 0$.

The altered Ekman solution is plotted with solid curves in Fig. 4 ⊙=, where U is chosen to match the along-isobath current above the boundary layer in the numerical solution. The standard Ekman solution ($\Delta z_0 = 0$) is plotted with dashed curves. The numerical result is close to the analytical solution (A1)–(A4), and the boundary layer is reasonably well resolved, indicating that the numerical model has formed an Ekman layer. The effect of the staggered grid is to raise the standard solution slightly above the bottom, but dynamically the Ekman layer behavior is unaltered.

Tables

Table 1. Parameters and properties of the downstream equilibrium estimated from numerical calculations, and used for comparison with the CL model in Fig. 15. Here, N ($\times 10^{-3}$ s^{-1}) is the buoyancy frequency, α the bottom slope, r (m s^{-1}) the bottom friction coefficient, W_n (km) the current width, δ_n (m) the maximum boundary layer thickness, u^i_n (m s^{-1}) the maximum along-isobath velocity on an s-coordinate surface just above the bottom boundary layer, and u^s_n (m s^{-1}) the maximum along-isobath surface velocity. In each case, the inflow has velocity $u_0 = 0.1$ m s^{-1} and width $2W_0 = 32.6$ km, and $f = 10^{-4}$ s^{-1}

Run	N	α	r	W_n	δ_n	u^i_n	u^s_n	$N\alpha/f$
1	9	0.001	0.002	77	47	0.031	0.039	0.09
2	9	0.002	0.002	50	42	0.060	0.059	0.18
3	9	0.002	0.001	48	43	0.058	0.054	0.18
4	18	0.001	0.001	56	24	0.061	0.059	0.18
5	14.3	0.001	0.001	63	31	0.048	0.055	0.143
6	6	0.002	0.002	64	67	0.037	0.046	0.12
7	18	0.001	0.0005	56	24	0.060	0.059	0.18
8	7.1	0.0014	0.002	68	55	0.036	0.042	0.10

Click on thumbnail for full-sized image.

Figures
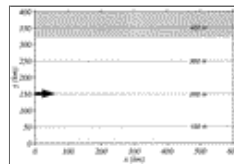
Click on thumbnail for full-sized image.

Fig. 1. Plan view of the numerical model domain. The arrow shows the location and direction of the imposed inflow. The shaded region is the location of a numerical sponge
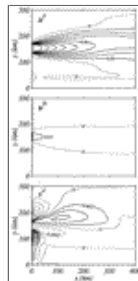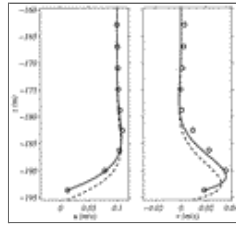

Click on thumbnail for full-sized image.

Fig. 2. Plan views of (upper) along-isobath surface velocity, (middle) along-isobath bottom velocity, and (lower) cross-isobath surface velocity for the standard calculation after 200 days. Parameters are $N = 9 \times 10^{-3}$ s^{-1}, $\alpha = 0.001$, $r = 0.002$ m s^{-1}, $u_0 = 0.1$ m s^{-1}, and $2W_0 = 32.6$ km. Contour intervals are 0.01 m s^{-1} for u^s and u^b, 0.0025 m s^{-1} for $\mathcal{U}^s$. The zero and negative contours are dotted
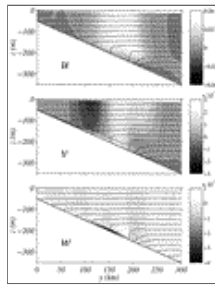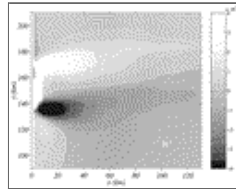
Click on thumbnail for full-sized image.

Fig. 3. Cross-isobath section of velocity components (gray shades) and density (black contours) for the standard calculation at $x = 300$ km after 200 days. Parameters are $N = 9 \times 10^{-3}$ s^{-1}, $\alpha = 0.001$, $r = 0.002$ m s^{-1}, $u_0 = 0.1$ m s^{-1}, and $2W_0 = 32.6$ km. Density contour interval is 0.2 kg m^{-3}. Velocity units are m s^{-1}. The white contours are zero velocity
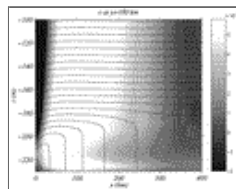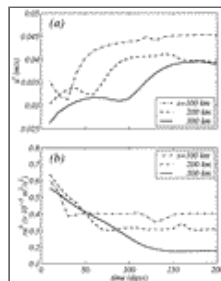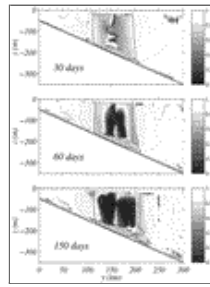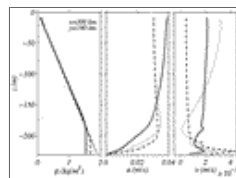

Click on thumbnail for full-sized image.

Fig. 4. Vertical profiles of horizontal velocities from (open circles) the standard calculation just downstream from the inflow ($x = 6$ km and $y = 145$ km) after 200 days, (solid curves) the Ekman solution appropriate for SPEM5.1 (see appendix), and (dashed curves) the standard Ekman solution. Parameters for the numerical solution are $N = 9 \times 10^{-3}$ s^{-1}, $\alpha = 0.001$, $r = 0.002$ m s^{-1}, $u_0 = 0.1$ m s^{-1}, and $2W_0 = 32.6$ km

Click on thumbnail for full-sized image.

Fig. 5. Plan view of vertical velocity (m s^{-1}) on an s-coordinate level, just above the bottom boundary layer, that slopes uniformly from $z = -114$ m at $y = 90$ km to $z = -218$ m at $y = 210$ km, from the standard calculation after 200 days. The white contour is $w = 0$. Parameters are $N = 9 \times 10^{-3}$ s^{-1}, $\alpha = 0.001$, $r = 0.002$ m s^{-1}, $u_0 = 0.1$ m s^{-1}, and $2W_0 = 32.6$ km

Click on thumbnail for full-sized image.

Fig. 6. Along-isobath section of cross-isobath velocity (gray shades in m s^{-1}) and density (black contours) from the standard calculation at $y = 180$ km after 200 days. Density contour interval is 0.05 kg m^{-3}. The white contour is $\mathbb{U} = 0$. Parameters are $N = 9 \times 10^{-3}$ s^{-1}, $\alpha = 0.001$, $r = 0.002$ m s^{-1}, $u_0 = 0.1$ m s^{-1}, and $2W_0 = 32.6$ km

Click on thumbnail for full-sized image.

Fig. 7. Time histories of (a) along-isobath surface velocity and (b) along-isobath bottom stress from the standard calculation at $y = 180$ km and $x = 100$, 200, and 300 km downstream. Parameters are $N = 9 \times 10^{-3}$ s^{-1}, $\alpha = 0.001$, $r = 0.002$ m s^{-1}, $u_0 = 0.1$ m s^{-1}, and $2W_0 = 32.6$ km
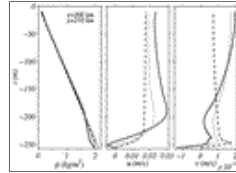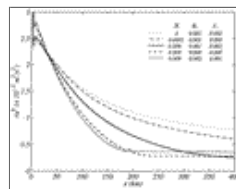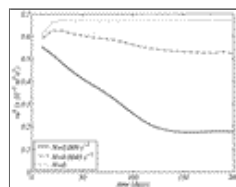

Click on thumbnail for full-sized image.

Fig. 8. Cross-isobath sections of the diagnostic for geostrophic flow along isopycnals, based on (12), for the standard calculation at $x = 100$ km and at the times indicated in each panel. Values of zero (black) indicate that (12) is satisfied, i.e., flow is geostrophic and along isopycnals. See text for more details. The black contour is $u = 0.01$ m s^{-1}. Parameters are $N = 9 \times 10^{-3}$ s^{-1}, $\alpha = 0.001$, $r = 0.002$ m s^{-1}, $u_0 = 0.1$ m s^{-1}, and $2W_0 = 32.6$ km

Click on thumbnail for full-sized image.

Fig. 9. Vertical profiles of density and horizontal currents from the downstream equilibrium of the standard calculation at $x = 300$ km and $y = 180$ km after (dashed) 50, (dotted) 100, and (solid) 200 days. The thin solid density curve is the initial profile. Parameters are $N = 9 \times 10^{-3}$ s^{-1}, $\alpha = 0.001$, $r = 0.002$ m s^{-1}, $u_0 = 0.1$ m s^{-1}, and $2W_0 = 32.6$ km

Click on thumbnail for full-sized image.

Fig. 10. As in Fig. 9 ⊙, except at $x = 300$ km and $y = 210$ km

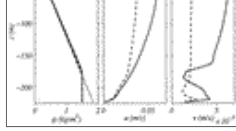Click on thumbnail for full-sized image.

Fig. 11. Steady-state along-isobath bottom stress beneath the core of the adjusting current, for several combinations of parameters. In each case, $u_0 = 0.1$ m s^{-1} and $2W_0 = 32.6$ km. The thick solid curve is the standard calculation
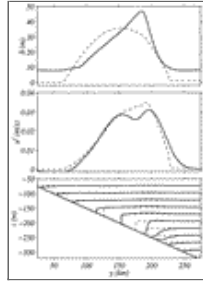

Click on thumbnail for full-sized image.

Fig. 12. Time histories of along-isobath bottom stress at $x = 300$ km and $y = 180$ km for various levels of stratification. Other parameters are $\alpha = 0.001$, $r = 0.002$ m s^{-1}, $u_0 = 0.1$ m s^{-1}, and $2W_0 = 32.6$ km

Fig. 13. Vertical profiles of density and horizontal currents from (dashed) the standard calculation ($u_0 = 0.1$ m s^{-1} and $2W_0 = 32.6$ km) and (solid) a narrower and stronger inflow ($u_0 = 0.2$ m s^{-1} and $2W_0 = 16.3$ km), each at $x = 300$ km and $y = 175$ km after 200 days. The thin solid density curve is the initial profile. Other parameters are $N = 9 \times 10^{-3}$ s^{-1}, $\alpha = 0.001$, and $r = 0.002$ m s^{-1}

Fig. 14. Comparison of (upper) bottom boundary layer thickness, (middle) along-isobath velocity just above the boundary layer, and (lower) density field for (solid) the standard calculation at $x = 300$ km after 200 days and (dashed) the downstream equilibrium of the idealized CL model. Parameters are $N = 9 \times 10^{-3}$ s^{-1}, $\alpha = 0.001$, $r = 0.002$ m s^{-1}, $u_0 = 0.1$ m s^{-1}, and $2W_0 = 32.6$ km
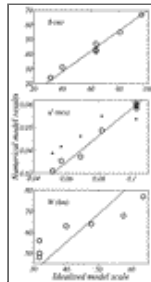
Fig. 15. Comparison of (upper) bottom boundary layer thickness;(middle) along-isobath velocity just above the boundary layer (circles) and at the surface (crosses); and (lower) current width in the downstream equilibrium of the numerical calculations with those predicted by the CL model from (14). The straight line in each panel is the least squares fit that passes through the origin
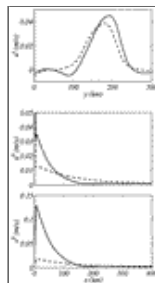
Fig. 16. (upper) Along-isobath surface velocity of the downstream equilibrium, and (middle) along-isobath, and (lower) cross-isobath bottom velocities beneath the core of the current, shown for (dashed) the standard calculation and (solid) one neglecting cross-isobath bottom stress, each after 200 days. The surface velocity is at $x = 300$ km for the standard calculation and at $x = 150$ km for the other calculation. Parameters are $N = 9 \times 10^{-3}$ s^{-1}, $\alpha = 0.001$, $r = 0.002$ m s^{-1}, $u_0 = 0.1$ m s^{-1}, and $2W_0 = 32.6$ km
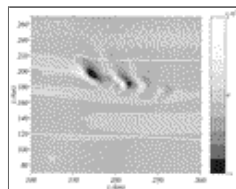
Fig. 17. Plan view of vertical velocity (m s^{-1}) on an s-coordinate level, just above the bottom boundary layer, that slopes

uniformly from $z = -102$ m at $y = 70$ km to $z = -281$ m at $y = 270$ km, from a higher resolution calculation with the standard parameters ($N = 9 \times 10^{-3}$ s^{-1}, $\alpha = 0.001$, $r = 0.002$ m s^{-1}, $u_0 = 0.1$ m s^{-1}, and $2W_0 = 32.6$ km) after 150 days. The white contour is the $u = 0.01$ m s^{-1}, which delineates the edges of the current. Note the small-scale, wave-like structures on the deep side of the current